FCS-MPC-Based Current Control of a Five-Phase Induction Motor and its Comparison with PI-PWM Control

Chee Shen Lim, *Student Member, IEEE*, Emil Levi, *Fellow, IEEE*, Martin Jones, Nasrudin Abd. Rahim, *Senior Member, IEEE*, and Wooi Ping Hew, *Member, IEEE*

***Abstract*—This paper presents an investigation of the finite-control-set model predictive control (FCS-MPC) of a five-phase induction motor drive. Specifically, performance with regard to different selections of inverter switching states is investigated. The motor is operated under rotor flux orientation, and both flux/torque producing $(d-q)$ and nonflux/torque producing $(x-y)$ currents are included into the quadratic cost function. The performance is evaluated on the basis of the primary plane, secondary plane, and phase (average) current ripples, across the full inverter's linear operating region under constant flux–torque operation. A secondary plane current ripple weighting factor is added in the cost function, and its impact on all the studied schemes is evaluated. Guidelines for the best switching state set and weighting factor selections are thus established. All the considerations are accompanied with both simulation and experimental results, which are further compared with the steady-state and transient performance of a proportional-integral pulsewidth modulation (PI-PWM)-based current control scheme. While a better transient performance is obtained with FCS-MPC, steady-state performance is always superior with PI-PWM control. It is argued that this is inevitable in multiphase drives in general, due to the existence of nonflux/torque producing current components.**

***Index Terms*—Current control, model predictive control (MPC), multiphase inverters, multiphase machines, weighting factor.**

I. Introduction

MULTIPHASE motor drives have received substantial attention during the last decade [1]. The good features of multiphase machines include low torque pulsations, means for inherently fault-tolerant operation, and better power distribution per phase [2]. A unique feature of multiphase machines, when compared with the conventional three-phase counterpart, is a higher number of degrees of freedom in electrical quantities [2].

Manuscript received May 9, 2012; revised August 15, 2012 and October 10, 2012; accepted November 27, 2012. Date of publication February 22, 2013; date of current version July 18, 2013.

C. S. Lim is with the Power Energy Dedicated Advanced Center (UMPEDAC), Wisma R&D, University of Malaya, 59990 Kuala Lumpur, Malaysia, and also with the School of Engineering, Technology and Maritime Operations, Liverpool John Moores University, Liverpool, L3 3AF, U.K. (e-mail: c.s.lim@2011.ljmu.ac.uk).

E. Levi and M. Jones are with the School of Engineering, Technology and Maritime Operations, Liverpool John Moores University, Liverpool, L3 3AF, U.K. (e-mail: e.levi@ljmu.ac.uk; m.jones2@ljmu.ac.uk).

N. A. Rahim and W. P. Hew are with the the Power Energy Dedicated Advanced Center (UMPEDAC), Wisma R&D, University of Malaya, 59990 Kuala Lumpur, Malaysia (e-mail: nasrudin@um.edu.my; wphew@um.edu.my).

Color versions of one or more of the figures in this paper are available online at http://ieeexplore.ieee.org.

Digital Object Identifier 10.1109/TIE.2013.2248334

In the field of power electronics and drives, model predictive control (MPC) has by now become an established control technique [3]. Previous MPC research in the multiphase drive area predominantly relates to the closed-loop current control of a dual three-phase (asymmetrical six-phase) induction machine with two isolated neutral points. Stationary $(\alpha-\beta-x-y)$ current control, with only switching states that correspond to the largest voltage vectors (and zero vector), was experimentally studied in [4]–[6]. However, the impact of using only the reduced set of switching states is not analyzed in detail. In [7] and [8], pulsewidth modulation (PWM) was integrated into the finite-control-set MPC (FCS-MPC) scheme(s) for the purposes of constant switching frequency and zeroing of average $x-y$ voltages. The same group of switching states, as in [4] and [5], was taken as the MPC's input set. A later work [9] has made an attempt to include all switching states in the MPC's optimization over a long time window. However, in each optimization cycle, a restrained search technique was introduced to enable on-the-fly switching state selection according to the predefined criteria, such as allowing only one commutation per inverter leg and no consecutive commutations in any leg. In other words, not all available switching states were considered by the MPC in each optimization cycle; instead, only 6, 11, or 16 switching states were included, depending on the predefined criteria. The search method reduced significantly the computational time of the FCS-MPC, which is usually high.

FCS-MPC has been also explored to some extent in conjunction with a five-phase induction motor drive. In [10], a predictive torque control algorithm is reported, and performance is experimentally investigated. Next, a synchronous current control scheme with a full set of switching states taken as the control input set of the FCS-MPC was addressed in [11] and [12], using simulation and experiments, respectively. Some other MPC-related works, which used a five-phase RL load, include [13] and [14]. Their focus was on algorithm's feasibility and simplification instead of drive's performance. Another study that used a five-leg inverter investigated the FCS-MPC-based current control of a two-motor three-phase motor drive with a common inverter leg [15]. That topology has the same number of electrical degrees of freedom as the five-phase and dual three-phase motor drives, i.e., four.

A multiphase system, even when supplied from a two-level inverter, is characterized by a high number of switching states. Space vector representation describes the multiphase system using multiple planes, i.e., primary $(\alpha-\beta)$ and secondary $(x-y)$

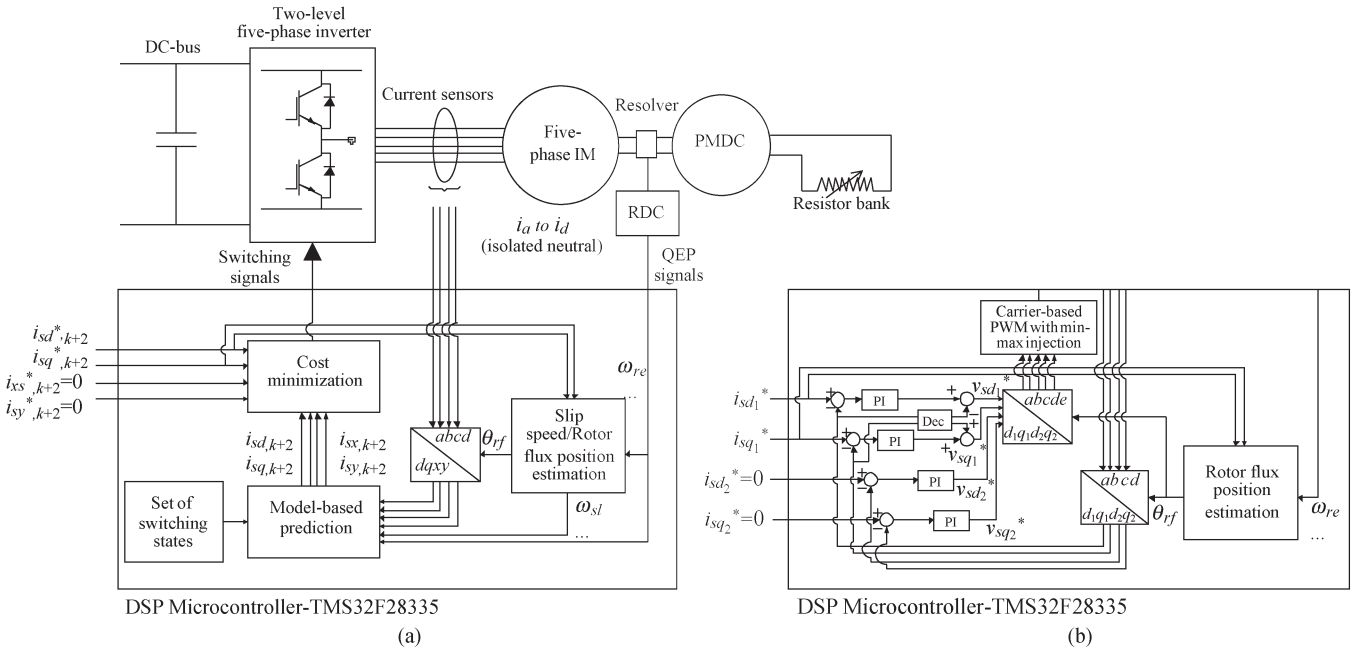

Fig. 1. Synchronous current control of a five-phase induction motor using (a) FCS-MPC and (b) the PI-PWM control. Both control schemes operate in the rotor flux reference frame and control all four axis components of the stator currents. "Dec." block corresponds to the standard voltage decoupling terms, i.e., $v_{sd,\mathrm{dec}} = \omega_{rf}\sigma L_s i_{sq}$ and $v_{sq,dec} = \omega_{rf} L_s i_{sd}$, where $\omega_{rf} = \omega_{re} + \omega_{sl}^*$.

planes. In a distributed-winding machine, only the primary plane is involved in the electromechanical energy conversion process while the secondary planes are not. Thus, the secondary plane currents are kept at zero, typically by using additional current controllers.

In this paper, the FCS-MPC with rotor field orientation applied to a five-phase induction motor with two-level voltage source inverter (VSI) supply is investigated. Both synchronous d- and q-axis currents and stationary x- and y-axis currents are considered by a single quadratic cost function. On the basis of the provided literature survey, it follows that the existing works have considered a significantly reduced set of inverter switching states as the input of the FCS-MPC-based current control scheme. No proper evaluation or comparison of the drive performance when all switching states and when reduced sets of switching states are used has ever been performed. Typical selection of only large vectors (plus zero vector) keeps the algorithm complexity at the minimum (comparable with a three-phase drive), and it is purely based on the intuitive reasoning that follows from five-phase inverter space vector PWM [16]: large voltage vectors of the flux/torque producing plane map into small voltage vectors in the nonflux/torque producing plane; hence, they will do the least damage with regard to excitation of the secondary plane currents. The first objective of this paper is, therefore, to investigate drive behavior when both the full and reduced sets of switching states are used.

The second objective is to investigate the impact of the weighting factor, which is introduced in the cost function to control the current errors in the nonflux/torque producing plane, on the overall drive performance. Such a weighting factor has already been used in some works [4], [8], [9], but its value appears to have always been selected in an *ad hoc* manner. The only previous papers where the issue has been studied to some extent were purely based on simulations [4], [11].

The considered schemes are compared on the basis of the primary plane, secondary plane, and phase current ripples, and the average switching frequencies of the schemes are also considered. The FCS-MPC based on the input switching state set that yields minimum current ripple is then selected for detailed evaluation, and its performance is compared with a proportional-integral PWM (PI-PWM) current control scheme in both steady-state and transient operations.

The rest of this paper is organized as follows: Section II describes the predictive model, cost function, control input set, performance criteria, and the PI-PWM current control design. Section III describes the current ripple investigation in relation to the control input set and weighting factor. Section IV shows the steady-state and transient comparison of the two control schemes and includes a study of the parameter detuning effects. Section V concludes the paper.

II. System Models and Other Considerations

The drive under consideration is illustrated in Fig. 1(a), which also corresponds to the experimental system layout.

It is well understood that the computational time of FCS-MPC is significant compared to the short sampling period in drive applications. Thus, it becomes improper to implement the optimization outcome within the same sampling period in which the mathematical optimization has been done. A common way to overcome this problem is by employing a two-step-ahead prediction strategy. This is, in essence, addition of one stage of prediction prior to execution of the MPC algorithm. This prediction is based on the feedback variables from measurements (some of them can be just predicted values) and the

known switching state that is being implemented. These first-step predicted variables will be used as the commencing state of the MPC algorithm, irrespective of the prediction horizon's length. Models and cost function in the MPC are given in what follows in discrete sampling step notation, accounting for the two-step-ahead prediction strategy.

A. Five-Phase Induction Motor Model

At sampling instant kT, where T is the sampling time, $X(k)$, which consists of measured (and transformed) axis currents and previously predicted rotor flux d-component, and $U(k)$, which consists of the axis voltages being applied from $t = kT$ to $t = (k+1)T$, are used to obtain the first-step predicted state $X(k+1)$. Next, this is used by the MPC algorithm, together with a set of axis voltages (control inputs) $U(k+1)$, to predict the first horizon axis currents that are required in the cost function. The axis voltages U are obtained from the inverter model in Section II-B. The predictive model is assumed to be time-invariant across the prediction horizon, which also means that the rotor (ω_{re}) and slip (ω_{sl}) speeds, which change with time, remain constant throughout the horizon. Thus, F_k at sampling time instant kT is used in the second-step prediction. The discrete state space model of the motor is

$$
\begin{aligned}
&X(k+2) = F_k \cdot X(k+1) + G \cdot U(k+1)\\
&Y(k+2) = H \cdot X(k+2)\\
&X(k+2) = [i_{sd,k+2} \quad i_{sq,k+2} \quad i_{sx,k+2} \quad i_{sy,k+2} \quad \lambda_{rd,k+2}]^T\\
&Y(k+2) = [i_{sd,k+2} \quad i_{sq,k+2} \quad i_{sx,k+2} \quad i_{sy,k+2}]^T\\
&U(k+1) = [v_{sd,k+1} \quad v_{sq,k+1} \quad v_{sx,k+1} \quad v_{sy,k+1}]^T\\
&F_k = \begin{bmatrix}
1+T\cdot A_1 & T\cdot A_2 & 0 & 0 & T\cdot A_3\\
-T\cdot A_2 & 1+T\cdot A_1 & 0 & 0 & -T\cdot A_4\\
0 & 0 & 1-\frac{T\cdot R_s}{L_{ls}} & 0 & 0\\
0 & 0 & 0 & 1-\frac{T\cdot R_s}{L_{ls}} & 0\\
\frac{T\cdot L_m}{T_r} & 0 & 0 & 0 & 1-\frac{T}{T_r}
\end{bmatrix}\\
&G = \begin{bmatrix}
\frac{T}{\sigma L_s} & 0 & 0 & 0\\
0 & \frac{T}{\sigma L_s} & 0 & 0\\
0 & 0 & \frac{T}{L_{ls}} & 0\\
0 & 0 & 0 & \frac{T}{L_{ls}}\\
0 & 0 & 0 & 0
\end{bmatrix}\\
&H = \begin{bmatrix}
1 & 0 & 0 & 0 & 0\\
0 & 1 & 0 & 0 & 0\\
0 & 0 & 1 & 0 & 0\\
0 & 0 & 0 & 1 & 0
\end{bmatrix}.
\end{aligned}
\tag{1}
$$

The coefficients are defined as

$$
\begin{aligned}
L_s &= L_{ls} + L_m & L_r &= L_{lr} + L_m\\
\sigma &= 1 - \frac{L_m^2}{L_s L_r} & A_1 &= -\left(\frac{1}{\sigma T_s} + \frac{1-\sigma}{\sigma T_r}\right)\\
& & A_2 &= \omega_{re,k} + \omega^*_{sl,k}\\
T_s &= \frac{L_s}{R_s} & A_3 &= \frac{1-\sigma}{\sigma L_m T_r}\\
T_r &= \frac{L_r}{R_r} & A_4 &= \frac{\omega_{re,k}(1-\sigma)}{\sigma L_m}
\end{aligned}
\tag{2}
$$

where R_s and R_r are stator and rotor winding resistances, respectively; L_{ls}, L_{lr}, and L_m are stator leakage inductance, rotor leakage inductance, and mutual inductance, respectively; T_s and T_r are stator and rotor time constants; and σ is the total leakage coefficient.

Model (1) is obtained by a forward-Euler discretization of the continuous time-domain model of the five-phase induction machine [1], which yields the discrete model in the rotating reference frame detailed in [12]. However, note that the q-axis rotor flux is not predicted in (1) as indirect rotor flux orientation principle is applied. The used slip speed in (1) and (2) is the feed-forward slip speed, so that the assumption of the zero q-axis rotor flux is indirectly included in the model. Based on model (1), control input at $t = (k+1)T$ will only affect the rotor flux vector components at $t = (k+3)T$, while the cost function considers only predicted variables at $t = (k+2)T$. Since neither measurements nor observer feedbacks are available to correct the rotor flux prediction, a possible approach to be considered in the future would be to include the predicted q-axis rotor flux component into the cost function, since its reference is always zero under field orientation. To do so, however, a minimum of two prediction horizons is required. This cannot be easily accomplished in multiphase drive applications, as hundreds/thousands of prediction and cost computations are required. The MPC without the prediction of the q-axis rotor flux has already been compared with the full model in [11], and no difference in the resulting performance was observed. As a result, the reduced model with one prediction horizon is adopted. A similar model was used in [17], but for a three-phase induction motor.

B. Five-Phase Inverter Model

Each two-level inverter leg has two switching states. Thus, for a five-phase VSI, there are 32 possible switching combinations. Each of the three MPC schemes, which will be described in Section II-D, uses a subset of the 32 switching states as its control input set.

A model of a five-phase inverter, which corresponds to $U(k+1)$ in (1), is presented next. At sampling instant kT, with one prediction horizon, the MPC is trying to find the switching state, which has the lowest cost at $t = (k+2)T$, to be implemented at $t = (k+1)T$. The speed of the synchronous (rotor flux) oriented reference frame, i.e., $\omega_{re,k} + \omega^*_{sl,k}$, is assumed to be constant. By applying decoupling transformation (C) and rotational transformation (R_{k+1}) [1] on machine phase-to-neutral voltages, $U(k+1)$ is obtained in the form:

$$
\begin{bmatrix} v_{sd,k+1}\\ v_{sq,k+1}\\ v_{sx,k+1}\\ v_{sy,k+1} \end{bmatrix}
= \frac{1}{5} V_{dc} R_{k+1} C \begin{bmatrix}
4 & -1 & -1 & -1 & -1\\
-1 & 4 & -1 & -1 & -1\\
-1 & -1 & 4 & -1 & -1\\
-1 & -1 & -1 & 4 & -1\\
-1 & -1 & -1 & -1 & 4
\end{bmatrix} \cdot \begin{bmatrix} s_A\\ s_B\\ s_C\\ s_D\\ s_E \end{bmatrix}
\tag{3}
$$

where $V_{\rm dc}$ is the dc-bus voltage, and $s_i = \{0, 1\}$ defines the ith inverter leg switching state, where $i = \{A, B, C, D, E\}$. Transformation matrices C and R_{k+1} are governed by

$$C = \frac{2}{5}\begin{bmatrix} 1 & \cos(\frac{2\pi}{5}) & \cos(\frac{4\pi}{5}) & \cos(\frac{6\pi}{5}) & \cos(\frac{8\pi}{5}) \\ 0 & \sin(\frac{2\pi}{5}) & \sin(\frac{4\pi}{5}) & \sin(\frac{6\pi}{5}) & \sin(\frac{8\pi}{5}) \\ 1 & \cos(\frac{4\pi}{5}) & \cos(\frac{8\pi}{5}) & \cos(\frac{2\pi}{5}) & \cos(\frac{6\pi}{5}) \\ 0 & \sin(\frac{4\pi}{5}) & \sin(\frac{8\pi}{5}) & \sin(\frac{2\pi}{5}) & \sin(\frac{6\pi}{5}) \end{bmatrix} \tag{4a}$$

$$R_{k+1} = \begin{bmatrix} \cos\theta_{rf,k+1} & \sin\theta_{rf,k+1} & 0 & 0 \\ -\sin\theta_{rf,k+1} & \cos\theta_{rf,k+1} & 0 & 0 \\ 0 & 0 & 1 & 0 \\ 0 & 0 & 0 & 1 \end{bmatrix} \tag{4b}$$

where $\theta_{rf,k+1}$ is the transformation angle at $t = (k+1)T$. The slip speed at sampling instant kT is calculated using (all variables with an asterisk in the superscript are the reference quantities)

$$\omega^*_{sl,k} = i^*_{sq,k} / \left(T_r i^*_{sd,k}\right). \tag{5}$$

$\theta_{sl,k}$ is obtained using trapezoidal rule, i.e.,

$$\theta_{sl,k} = \theta_{sl,k-1} + \frac{1}{2}T \cdot \left(\omega^*_{sl,k-1} + \omega^*_{sl,k}\right). \tag{6}$$

The rotor flux position at sampling instant kT is

$$\theta_{rf,k} = \theta_{re,k} + \theta_{sl,k}. \tag{7}$$

$\theta_{rf,k}$ is also used for rotational transformation of measured phase currents at sampling instant kT, to form part of the state variables $X(k)$. Since ω_{re} and ω^*_{sl} are constant throughout the prediction horizon, $\theta_{rf,k+1}$ is obtained using

$$\theta_{rf,k+1} = \theta_{rf,k} + T \cdot \left(\omega_{re,k} + \omega^*_{sl,k}\right). \tag{8}$$

Note that, if a longer prediction horizon (> 1) is desired, a proper formulation of future horizon synchronous reference frame voltages (in cases of synchronous current control) or future horizon stationary current references (in cases of stationary current control with field orientation) is necessary, with attention being paid to the future rotational transformation angle. Expression (8) is only applicable for the first horizon's rotational transformation.

It is to be noted that the zero switching states "00000" and "11111" are redundant states. Thus, only one of them is considered in the MPC optimization process ("00000" is selected). In implementation, however, whenever a zero switching state is required, the one that requires a lower number of commutations will be applied. For example, following two-step-ahead prediction time notation, if switching state "01111" is being realized at $t = kT$ and a zero switching state has been chosen to be implemented at $t = (k+1)T$, then "11111" is preferred over "00000."

C. Cost Function and W_{xy} Weighting Factor

Once when the prediction and control time horizons are set, the cost function remains as the only tuning tool that exists in the MPC. Typically, two forms of cost function are used, i.e., linear and quadratic. In this paper, there are four current error terms and up to 32 switching states to be considered. The x- and y-axis current control is necessary to eliminate low-order current harmonics that can be caused by dead time and machine asymmetry [18]. The quadratic form is chosen here as it can provide better insight into the cost values [19], particularly in more complex optimization problems such as this one. The cost function J is defined as

$$J = \left(i^*_{sd,k+2} - i_{sd,k+2}\right)^2 + \left(i^*_{sq,k+2} - i_{sq,k+2}\right)^2 + W_{xy}\left[\left(i^*_{sx,k+2} - i_{sx,k+2}\right)^2 + \left(i^*_{sy,k+2} - i_{sy,k+2}\right)^2\right]. \tag{9}$$

References for $x{-}y$ currents in (9) are identically equal to zero at all times. A W_{xy} weighting factor is introduced to alter (typically to lower) the importance of the secondary $(x{-}y)$ plane currents with respect to the primary $(d{-}q)$ plane currents. The need for this weighting factor stems from the nature of a five-phase inverter, where each active space vector maps into both planes [16], according to Fig. 2. If PWM is used, the average voltage in the $x{-}y$ plane can be easily zeroed by using four active vectors and a zero vector in each switching period [16]. However, in FCS-MPC, there is no modulation, and every chosen switching state is applied across a fixed time period. This produces, per sampling period, average voltages in both planes. The same applies to the case when two switching states per sampling period are used (see the FCS-MPC of a dual three-phase drive in [6]). On the other hand, flux/torque producing currents in the primary plane have higher priority than those in the secondary plane(s). Hence, weighting factor W_{xy} has to be properly adjusted, so that the drive gives a good output torque quality but with reasonably small secondary plane current ripples. Setting a lower W_{xy} allocates the higher effort and resource from the VSI toward the currents in the primary plane than the secondary plane(s).

A straightforward implication of this discussion is that the current ripple performance of the FCS-MPC in a multiphase drive will be only comparable with the standard control scheme with PWM if a much higher sampling frequency (and higher switching frequency) is used. This is, however, constrained by the computational burden due to the high number of switching states.

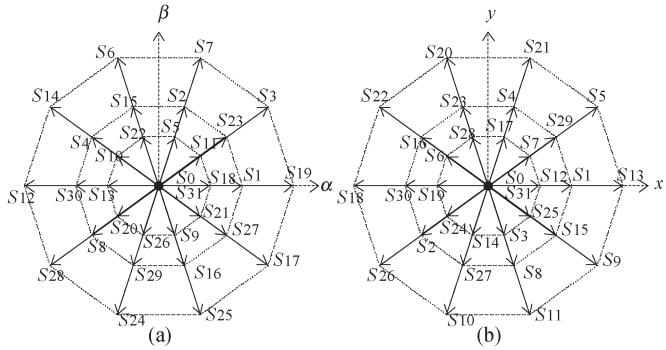

Fig. 2. Projections of inverter voltage space vectors in the two planes for vectors used in the three MPC schemes in Table II.

TABLE I
SPACE VECTOR GROUPS AND CORRESPONDING SWITCHING STATES

Group	Switching state
S	S_{18}, S_{11}, S_5, S_{22}, S_{10}, S_{13}, S_{20}, S_{26}, S_9, S_{21}
M	S_1, S_{23}, S_2, S_{15}, S_4, S_{30}, S_8, S_{29}, S_{16}, S_{27}
L	S_{19}, S_3, S_7, S_6, S_{14}, S_{12}, S_{28}, S_{24}, S_{25}, S_{17}
Zero	S_0, S_{31}

TABLE II
CONSIDERED FCS-MPC SCHEMES WITH REGARD TO THE SWITCHING STATE SETS

Scheme	Group
MPC-31	*S*+ *M* + *L* + *Zero*
MPC-21	*M* + *L* + *Zero*
MPC-11	*L* + *Zero*

D. Input Switching State Sets and MPC Schemes

The voltage vectors of the 32 switching states are decomposed into the primary and secondary planes using vector space decomposition matrix C of (4a) in complex form. Their projections in the two planes are shown in Fig. 2. The switching states are categorized, based on the primary plane voltage vectors' magnitude, into groups of S (small), M (medium), L (large), and $Zero$, as summarized in Table I. Three FCS-MPC schemes that use different combinations of these switching states are studied further on. The FCS-MPC that uses all the $(S+M+L+Zero)$ switching states is termed as MPC-31. Next, it has been demonstrated in a previous work [5] with dual three-phase drive that an equivalent $(L+Zero)$ switching state set is feasible. Hence, a similar scheme is studied here for a five-phase drive (MPC-11). Finally, it has been shown in [11] that FCS-MPC occasionally uses only two adjacent sets of active switching states; thus, MPC-21, which uses $(M+L+Zero)$ switching states, is introduced and investigated as the third possible choice. The schemes are summarized in Table II. They are compared on the basis of the primary plane, secondary plane, and average phase current ripples. An effort has also been made to compare their average switching frequency.

E. Performance Criteria

The primary plane $(d-q)$ current ripple is defined as

$$\frac{1}{\sqrt{2}}\sqrt{[\text{RMS}\,(i_{sd}-\text{mean}(i_{sd}))]^2+[\text{RMS}\,(i_{sq}-\text{mean}(i_{sq}))]^2}. \tag{10}$$

The mean values of the d- and q-axis currents in (10) essentially represent dc-component equivalents of the fundamental harmonic in the primary plane. Thus, removing them from the primary plane d- and q-axis currents yields the higher order harmonics, or ripple. Next, the secondary plane $(x-y)$ current ripple is defined as

$$\frac{1}{\sqrt{2}}\sqrt{[\text{RMS}(i_{sx})]^2+[\text{RMS}(i_{sy})]^2} \tag{11}$$

where it is assumed that the mean values of x- and y-axis currents are always zero. Since phase currents of the machine do not have identical harmonic content, only the average phase current ripple can be determined, and it is defined as (12), as shown at the bottom of the page. The current samples for the ripple calculations are obtained from a common time window that contains an integer multiple of the fundamental period.

Considering that the induction motor is vector-controlled with constant flux current, which here has a comparable magnitude with the torque current, the fundamental current has relatively small amplitude change throughout the operating range. In contrast, the fundamental frequency changes in a wide range, i.e., 0–50 Hz. In addition, the stator fundamental frequency indirectly determines the composition of the applied active vectors from the groups of S, M, and L [11]. Hence, a comparison of performance of all the FCS-MPC schemes is done with respect to the stator fundamental frequency (which governs the required fundamental voltage), rather than current, using a variable weighting factor in (9).

F. Current Control With PI-PWM

Ideally, a distributed winding five-phase inductor motor can be controlled by using only one pair of PI controllers for the primary plane $(d-q)$ currents. However, it has been shown in [18] that numerous nonideal properties can cause the flow of the undesired secondary plane $(x-y)$ currents. Even with a perfectly symmetrical machine, inverter dead-time effect will inevitably cause low-order harmonics in the secondary plane. An alternative, based on the use of two pairs of current controllers, both operated in the synchronous reference frame, was therefore suggested in [18] as a solution, and this current control scheme is adopted here. Hence, two pairs of current controllers are utilized to improve the output current quality.

The complete PI-PWM control scheme is depicted in Fig. 1(b). The PI-PWM control is implemented in the rotor-flux-oriented reference frame, with the transformation angle obtained using the standard feed-forward (indirect) field-oriented control, as in (5) and (6). The stationary axis current components are obtained from the measured phase currents using the decoupling transformation (4a). Next, the primary plane stationary axis currents $i_{s\alpha}$ and $i_{s\beta}$ are rotationally transformed to the primary plane synchronous axis current components i_{sd1} and i_{sq1}. These transformed currents are controlled by the first pair of PI controllers, which thus govern flux and torque production. The secondary plane current components i_{sx} and i_{sy} are also transformed to the same rotating reference frame,

$$\frac{1}{\sqrt{2}}\sqrt{[\text{RMS}\,(i_{sd}-\text{mean}(i_{sd}))]^2+[\text{RMS}\,(i_{sq}-\text{mean}(i_{sq}))]^2+[\text{RMS}(i_{sx})]^2+[\text{RMS}(i_{sy})]^2} \tag{12}$$

TABLE III
PARAMETERS RELEVANT TO THE MPC ALGORITHMS

Parameter	Value
Sampling period	100 μs
Dc-link voltage	400 V
IM stator phase resistance R_s	2.8 Ω
IM stator leakage inductance L_{ls}	45 mH
IM mutual inductance L_m	505 mH
IM rotor phase resistance R_r	1.6 Ω
IM rotor leakage inductance L_{lr}	15 mH
IM rated frequency	50 Hz
IM pole pairs	2

to form i_{sd2} and i_{sq2}. The complete rotational transformation matrix is [18]

$$R = \begin{bmatrix} \cos\theta_{rf} & \sin\theta_{rf} & 0 & 0 \\ -\sin\theta_{rf} & \cos\theta_{rf} & 0 & 0 \\ 0 & 0 & \cos\theta_{rf} & \sin\theta_{rf} \\ 0 & 0 & -\sin\theta_{rf} & \cos\theta_{rf} \end{bmatrix}. \quad (13)$$

It is well known that FCS-MPC has the fast dynamic control ability. Therefore, to give fair comparison, the PI-PWM control scheme is complemented with the standard stator voltage decoupling terms, in order to improve its dynamic performance. The output of the PI-PWM control scheme consists of both planes' synchronous voltage references, which are rotationally transformed back into the stationary reference frame. Phase voltage references are formed next, and the PWM modulator used is that of the carrier-based type with min–max injection.

The proportional and integral coefficients of the four PI controllers are tuned using simulation and further fine-tuned experimentally. The same values are used for each pair of the current controllers in the simulations and experiments.

III. CONTROL INPUT SET AND WEIGHTING FACTOR

A dc-bus voltage of 400 V is used. The flux (d-axis) current is set to $\sqrt{2}$ A (no-load magnetizing current at rated voltage). The torque (q-axis) current is limited to $\sqrt{2}$ A. The x- and y-axis current references are set to zero. Under the given conditions and on the basis of the machine data (see Table III), the fundamental frequency of the machine is theoretically limited to the range of 0–40 Hz, to keep the inverter in the linear operation (or, equivalently, in the linear modulation region), in order to avoid excessive currents in the $x-y$ plane.

The control algorithms are experimentally realized using a five-phase induction motor, a laboratory prototype of a two-level five-phase inverter, and a floating-point microcontroller TMS320F28335 (residing in an ezdsp28335 kit). The inverter is built from Semikron dual insulated-gate-bipolar-transistor modules SKM100GB12T4 (1200 V, 100 A). Four phase currents are measured using current sensors LEM LA55P, and the obtained outputs are buffered to the analog-to-digital converter peripheral of the microcontroller. The rotor speed is measured using a resolver, and the output signal is converted to quadrature-encoder-pulse (QEP) type using a resolver-to-digital converter (AD2S90). The emulated QEP signal is fed to the eQEP peripheral of the microcontroller. As the standard symmetrical carrier way of gate signal generation is not suitable for FCS-MPC, the ePWM peripheral has additionally been modified to provide full controllability of the output gating signals. The dead time, which was neglected in the simulations, is set to 4 μs.

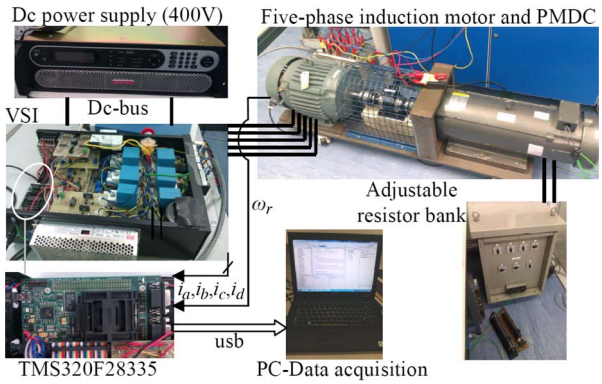

Fig. 3. Overall experimental setup (PMDC denotes permanent magnet dc motor, which is operated as a generator).

A. Machine Loading and Data Acquisition

The five-phase induction motor is mechanically coupled to a permanent magnet dc generator (PMDC). Armature of the PMDC is connected to a variable resistor bank. Given a constant driving torque from the induction motor, the rotor speed (and hence the stator fundamental frequency due to constant flux–torque operation) can be adjusted almost linearly by the load resistance value. In the experiments, the induction motor is operated in the torque mode (no closed-loop speed control). This enables a fair evaluation of the FCS-MPC performance when used as the current controller. The experimental setup is shown in Fig. 3. Table III shows the relevant parameters and conditions that are used in the experimental predictive model (and also in simulations).

The current measurements are sampled at 10 kHz by the DSP. Four currents are measured, and this subsequently allows the computation of stationary axis and synchronous axis current components. Once when the data have been acquired, they are plotted using a MATLAB plotting tool. On the other hand, fast Fourier transform (FFT) of phase currents is directly performed using an Agilent dynamic signal analyzer 35670 A, and the obtained current spectrum is acquired and also replotted using the MATLAB plotting tool. For better accuracy, the highest number of lines (1600) and an integer number of fundamental cycles of current samples in the acquisition window are ensured. The latter minimizes any potential spectral leakage phenomenon.

B. Nonideal Properties in the Experiment

Some nonideal properties of the machine and the other components in the experimental setup will lead to certain discrepancies between the simulation and experimental results, as shown shortly. In the experimental study, the stator fundamental frequency is limited to the range of 0–35 Hz, since 40 Hz is not realizable if linear inverter operation is to be maintained with the given 400-V dc-bus voltage and $\sqrt{2}$-A flux current. In essence, inverter dead time reduces the realizable maximum fundamental voltage and is the source of this difference.

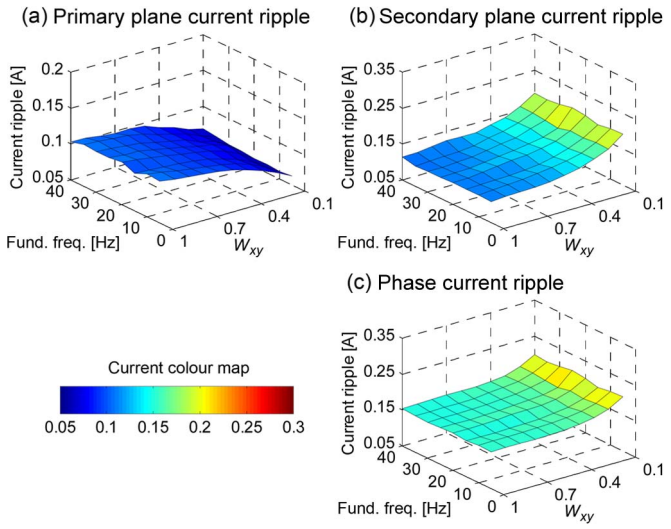

Fig. 4. (Simulation) Summary of ripple characteristics of (a) the primary plane currents, (b) the secondary plane currents, and (c) the average phase current of MPC-31 from 5- to 40-Hz stator fundamental frequencies with W_{xy} varying from 0.1 to 1 ($i^*_{sd} = i^*_{sq} = \sqrt{2}$ A and $i^*_{sx} = i^*_{sy} = 0$ A).

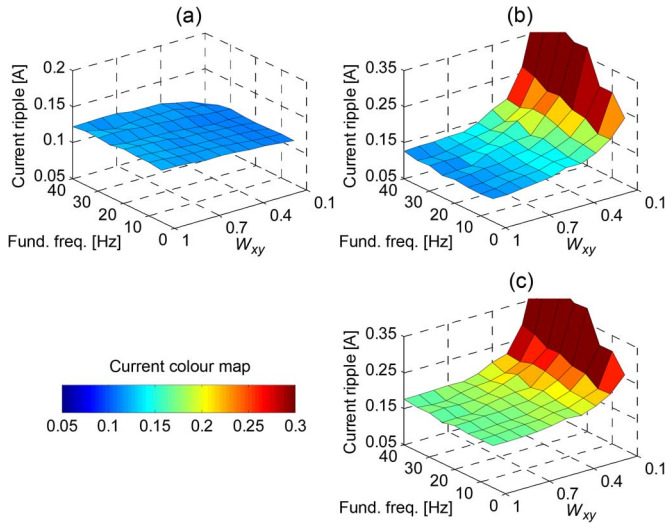

Fig. 5. (Simulation) Summary of ripple characteristics of (a) the primary plane currents, (b) the secondary plane currents, and (c) the average phase current of MPC-11 (conditions as in Fig. 4).

Existence of dead time causes higher ripple in the plane currents, particularly in the secondary plane, due to the low leakage inductance [18]. Additionally, in the machine used, there is a pronounced rotor slot harmonic effect, particularly at high load operation. The model of the machine, used in the FCS-MPC, does not account for these nonideal properties, which however cause higher current ripples in the experimental results.

C. Simulation and Experimental Results

The performance of the FCS-MPC is evaluated, based on the current ripples, against varying stator fundamental frequency and weighting factor W_{xy}. The simulations have been done from 5 to 40 Hz with 5-Hz increments. Instants of constant load torque application to the machine are varied, so that the desired rotor speeds and thus the stator frequencies are obtained. Weighting factor W_{xy} is varied from 0.1 to 1 in steps of 0.1 for each fundamental frequency, in all the schemes. The selection of 10 kHz as the MPC sampling period is based on the shortest period achievable by the DSP in the experiments for the most computationally demanding scheme, i.e., MPC-31.

Figs. 4 and 5 show the 3-D plots of current ripples in MPC-31 and MPC-11, respectively. The effect of the stator fundamental frequency on the current ripple characteristics is not pronounced, except in MPC-11 at low W_{xy} (0.1–0.2). As the stator fundamental frequency increases, the required stator fundamental voltage increases as well, but the stator fundamental frequency still has insignificant impact on the plane and phase current ripples.

Weighting factor W_{xy} has more pronounced impact than the stator fundamental frequency on all the schemes. Fig. 4(a) and (b) show that, as W_{xy} in the MPC-31 decreases from 1 to 0.1, the primary plane current ripple decreases by about 40%, while the secondary plane current ripple increases by about 70%. This results in an increase in the average phase current ripple by approximately 30% [see Fig. 4(c)]. However, the phase current ripple remains essentially constant for W_{xy} from 1.0 to 0.5. In other words, setting of W_{xy} as 0.5 can result in, without increase in the overall phase current ripple, redistribution of some current ripple from the primary plane to the secondary plane. This favors the objective of better torque quality. W_{xy} can be further reduced if better ripple behavior of the primary plane currents and torque is required, but at the expense of higher secondary plane current ripple.

To the contrary, tuning of W_{xy} in MPC-11 appears to be unnecessary, since the value of 1 is optimal. Fig. 5(a) and (b) show that the primary plane current ripple remains about the same throughout the range of W_{xy}, but the secondary plane current ripple increases with W_{xy} decrease nearly two times. The phase current ripple [see Fig. 5(c)] increases in a similar manner. Hence, there appears to be no reason to use smaller W_{xy} as the best control outcome is obtained at equal-plane weighting condition, i.e., $W_{xy} = 1$. This value does fit with the one used in an *ad hoc* manner in [5] and [6]. The primary plane and phase current ripples of MPC-11, even with $W_{xy} = 1$, are still significantly higher than for MPC-31.

Next, the plane and phase current ripples of MPC-21 are shown in Fig. 6. They have, for all practical considerations, the same behavior as MPC-31 not only in both planes individually, but for the average phase current ripple as well. This implies that the S group of switching states does not need to be included in the control input set.

Fig. 7 shows the experimentally obtained current ripples for MPC-31. Plane and phase current ripples show slight dependence on the stator fundamental frequency, which was not evident in the simulation results. This is explained by the nonideal properties (dead time and rotor slot harmonics) that are present in the experiment. At $W_{xy} = 1$, both plane current ripples have similar magnitude. The primary plane current ripple decreases by about 30% while the secondary plane current ripple increases by about 75% as W_{xy} changes from 1 to 0.1, while the average phase current ripple increases

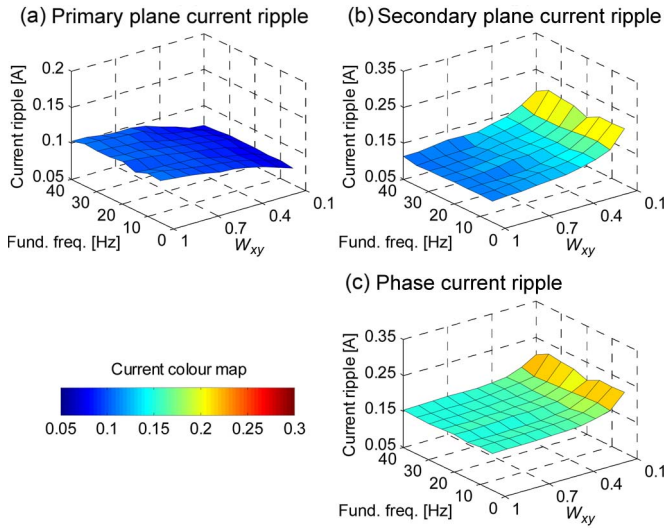

Fig. 6. (Simulation) Summary of ripple characteristics of (a) the primary plane currents, (b) the secondary plane currents, and (c) the average phase current of MPC-21 (conditions as in Fig. 4).

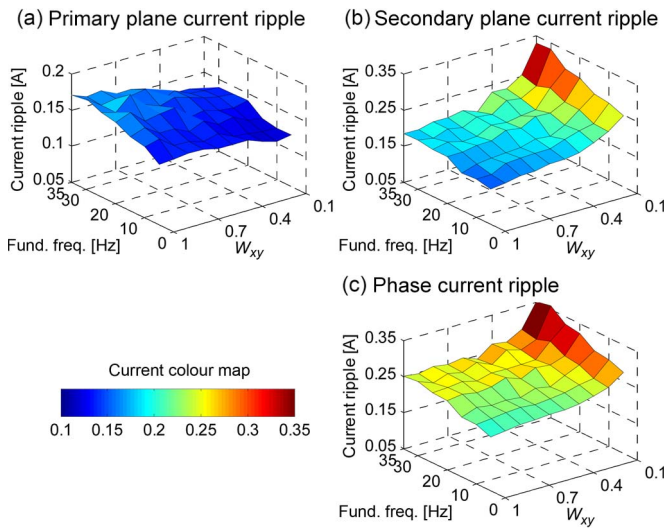

Fig. 7. (Experiment) Summary of ripple characteristics of (a) the primary plane currents, (b) the secondary plane currents, and (c) the average phase current of MPC-31 from 5- to 35-Hz stator fundamental frequencies with W_{xy} varying from 0.1 to 1 ($i_{sd}^* = i_{sq}^* = \sqrt{2}$ A and $i_{sx}^* = i_{sy}^* = 0$ A).

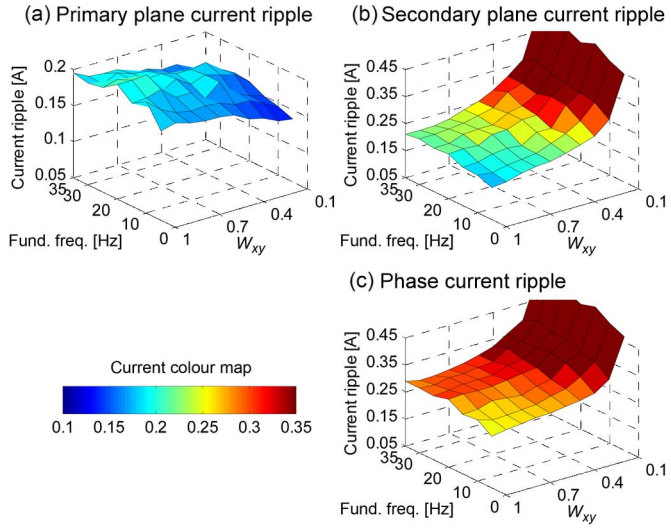

Fig. 8. (Experiment) Summary of ripple characteristics of (a) the primary plane currents, (b) the secondary plane currents, and (c) the average phase current of MPC-11 (conditions as in Fig. 7).

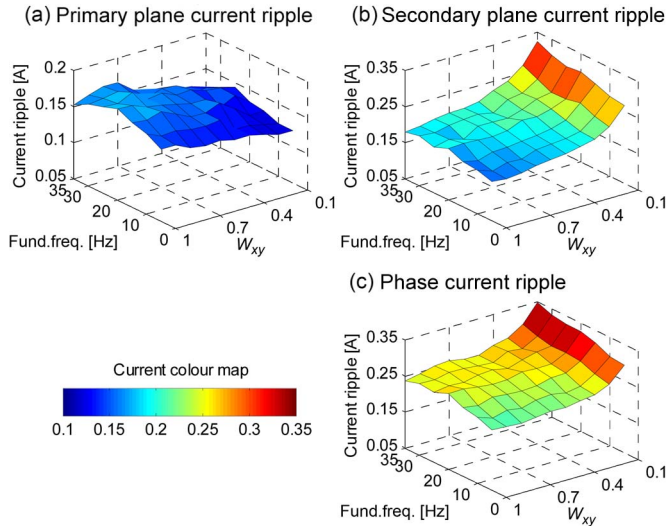

Fig. 9. (Experiment) Summary of ripple characteristics of (a) the primary plane currents, (b) the secondary plane currents, and (c) the average phase current of MPC-21 (conditions as in Fig. 7).

by approximately 35% [see Fig. 7(c)]. The experimental results confirm the finding of the simulation study that decreasing W_{xy} from 1 to 0.5 reduces the primary plane current ripple while keeping the average phase current ripple practically unchanged. The experimental 3-D plots in Fig. 7 closely follow the trends of the simulation results in Fig. 4, while there is an upward shift in the actual ripple values, attributed to the phenomena that are not modeled.

Fig. 8 shows the experimental results for MPC-11. The primary plane current ripple [see Fig. 8(a)] depends marginally on W_{xy}, i.e., the ripple slightly decreases with decreasing W_{xy}, in contrast to the independence in the simulation. The primary current ripple is still always higher in MPC-11 than in MPC-31, thus confirming the simulation findings. The secondary plane current ripple [see Fig. 8(b)] shows the same behavior with regard to W_{xy} dependence, as in the simulation results in Fig. 5(b). Similarly, the average phase current ripple increases drastically with reduction in W_{xy}, thus showing a good agreement with Fig. 5(c). Hence, the weighting factor of MPC-11 has to be kept around the value of 1, to avoid exceptionally high secondary plane and, consequently, phase current ripples.

Results for the MPC-21 are summarized in Fig. 9. It can be seen that current ripples are for all practical purposes the same as with MPC-31 in Fig. 7. This confirms that the S-group switching states can be excluded, even in the actual implementation, regardless of the nonideal properties of the drive system.

For all the schemes, there is no dynamic restriction on how the voltage vector can change, i.e., no imposed restriction on the future selectable switching states [9] or voltage vectors [20], in relation to the previous/present ones. There is also no switching-stress-related term in the cost function. For these reasons, all the schemes will have a very similar transient

TABLE IV
COMPARISON OF AVERAGE SWITCHING FREQUENCY FOR MPC-31, MPC-21, AND MPC-11

Schemes	Simulation	Experiment
MPC-31	650-2600	1950-3700
MPC-21	650-2300	1950-3500
MPC-11	600-2300	1850-3300

performance and the same maximum switching frequency of $f/2$ (where f is the sampling frequency). However, the typical average switching frequency of FCS-MPC usually remains around $0.2f-0.3f$, depending on the operating point. Table IV summarizes the range of average switching frequency for all considered schemes, which was obtained in the simulations and experiments. For all schemes, the switching frequency is higher in the experiments than in the simulations. This is in fact expected due to the discussed nonideal properties of the system.

Another important observation is that, although MPC-11 uses only the smallest $x-y$ voltage vectors, the resulting secondary plane current ripples are still slightly higher than with the other two schemes, even at $W_{xy}=1$. This is evident in both the simulation (see Fig. 5) and experimental (see Fig. 8) results. As a conclusion, it follows that using only $(L+Zero)$ vectors in FCS-MPC (the most common approach until now) does not result in the lowest current ripple. It is therefore recommended to include at least the switching states of $(M+L+Zero)$ groups in the input set of the predictive controller, for the best compromise between the performance and complexity. This is, in a way, an expected conclusion, since the standard PWM for five-phase VSIs [16] also uses $(M+L+Zero)$ switching states without any S vectors.

IV. COMPARISON WITH PI-PWM CONTROL

A. Conditions of Comparisons

It has been concluded in Section III-C that MPC-31 and MPC-21 give practically the same performance, although the latter uses a smaller input set. Nevertheless, to ensure that the best possible performance of the FCS-MPC is compared with the PI-based current control, MPC-31 is used here. The W_{xy} factor is set to 0.5, since it has been concluded that this value gives practically the same phase current ripple as the case with $W_{xy}=1$, with 15% smaller primary plane current ripples but 15% higher secondary plane current ripples.

For PI-PWM control, coefficients for the primary plane current (i_{sd1} and i_{sq1}) controllers are set as equal, i.e., $k_{p1}=1$ and $k_{i1}=0.01$, whereas coefficients for the secondary current (i_{sd2} and i_{sq2}) controllers are $k_{p2}=0.5$ and $k_{i2}=0.01$. The PWM switching frequency is set to 2.5 kHz [roughly the midpoint value of the MPC-31 experimental average switching frequencies of 1.95–3.7 kHz (see Table IV)]. The current ripple performance of the two control schemes in steady state is compared first.

B. Steady-State Performance Comparison

The current ripples of both control schemes are studied by simulation and experimentally. The drive is operated in constant flux–torque mode with current references of $i^*_{sd}=i^*_{sq}=\sqrt{2}$ A ($i^*_{sd1}=i^*_{sq1}=\sqrt{2}$ A) and $i^*_{sx}=i^*_{sy}=0$ A ($i^*_{sd2}=i^*_{sq2}=0$ A). Fig. 10 summarizes the obtained primary plane, secondary plane, and average phase current ripples for the MPC-31 with $W_{xy}=0.5$ and the PI-PWM control for different operating frequency. It should be noted that the average phase current ripple can be related to the current total harmonic distortion (THD) due to common fundamental current magnitude (constant current references).

Fig. 10 shows that the operating frequency (i.e., stator fundamental frequency) affects the resulting current ripple characteristic of the PI-PWM control, which was obtained by simulation, significantly. The primary plane current ripple varies only slightly, but the secondary plane current ripple

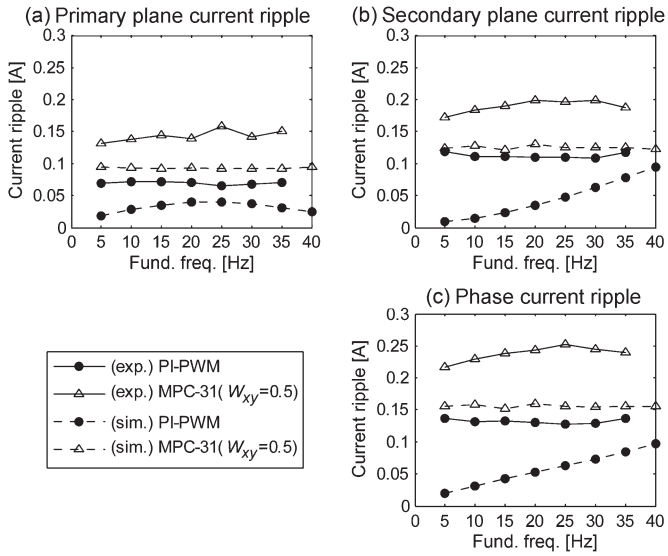

Fig. 10. (Simulation and experiment) Comparison of (a) the primary plane current ripple, (b) the secondary plane current ripple, and (c) the average phase current ripple for the MPC-31 and PI-PWM control. The data apply to the same conditions as in Figs. 4–9.

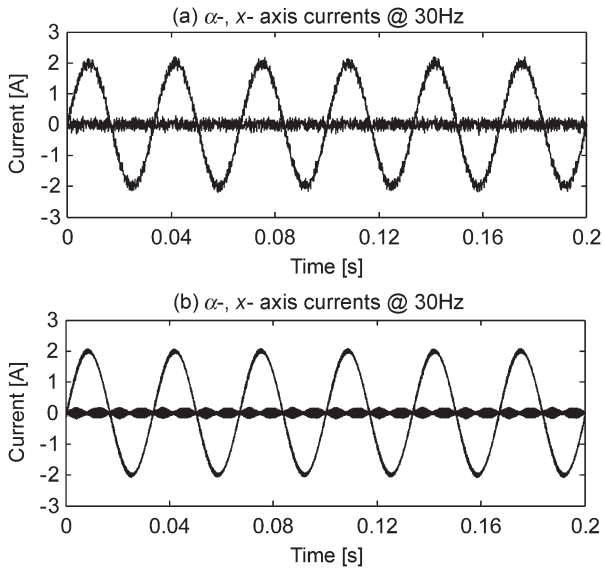

Fig. 11. (Simulation) Steady-state α- and x-axis currents for (a) MPC-31 with $W_{xy}=0.5$ and (b) PI-PWM control at 30-Hz stator fundamental frequency (current references as in Fig. 4).

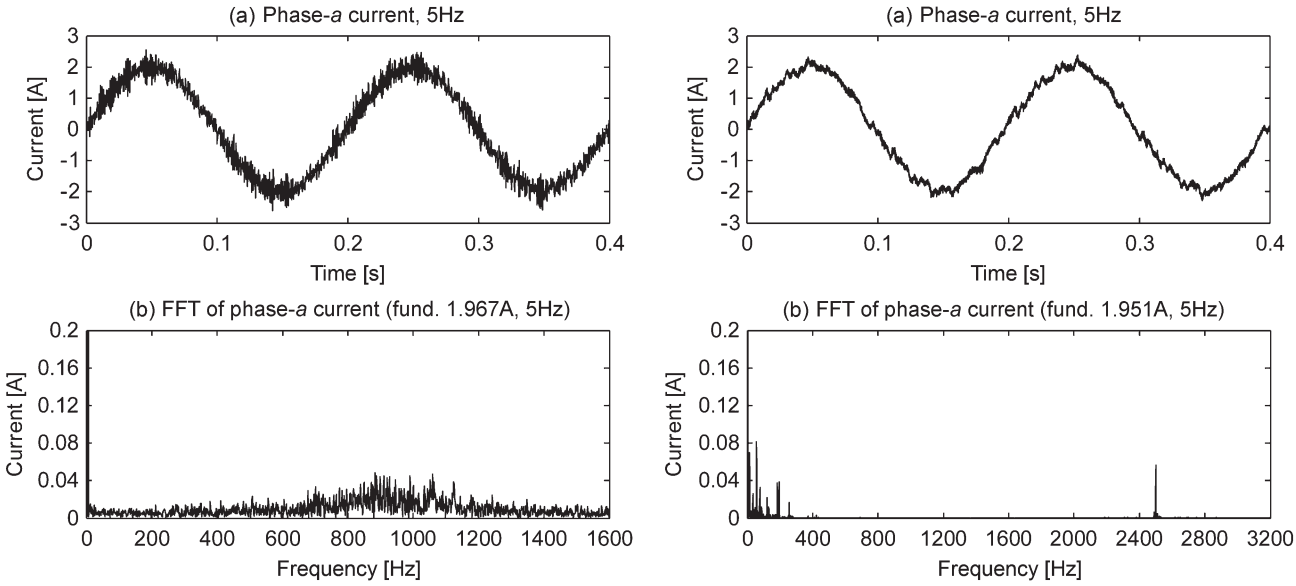

Fig. 12. (Experiment) Comparison of steady-state currents at 5-Hz operation. The machine is loaded with the same load torque as in Fig. 7. (a) Phase-a current waveform. (b) FFT of the phase-a current. MPC-31 results are on the left, whereas PI-PWM results are on the right.

increases with an increase in the operating frequency. The phase current ripple increases almost linearly by 400% with the operating frequency. It is worth mentioning that the current ripple characteristic is dependent on the utilized PWM technique. The PWM utilized here gives practically the same ripple characteristic as does the space vector PWM, which is based on the use of two large and two medium voltage vectors in each switching period [16], [21] (the current ripple study in [21] utilized the same five-phase induction machine as used here).

In general, MPC-31 gives higher current ripple than PI-PWM control in simulations. It should be noted that the range of the MPC-31's average switching frequency is, in simulations, only 0.65–2.6 kHz, whereas the PI-PWM control operates with 2.5-kHz switching frequency. A much better simulation ripple performance is attained by the PI-PWM control, particularly at low operating frequency at the expense of higher switching stress. Nevertheless, one should notice that, at a 30-Hz operating point, the two control schemes have almost the same average switching frequencies (2.25 versus 2.5 kHz), but the PI-PWM control still excels over the MPC-31 by 112% in the phase current ripple. The corresponding time-domain α- and x-axis current waveforms are shown in Fig. 11.

Fig. 10 also includes the experimental results. The current ripples of MPC-31 are consistently higher than those of the PI-PWM control and this agrees with the trend in the simulation results, although the experimental values are higher. However, experimental results do not show frequency dependence of ripple for PI-PWM control in the second plane and hence in the phase current as well. This is believed to be due to the already mentioned unmodeled phenomena (dead time and rotor slot harmonics).

Figs. 12(a) and 13(a) show the experimental phase-a currents for both control schemes at 5- and 30-Hz operations, respectively, with Figs. 12(b) and 13(b) showing their spectra. The fundamental components (values of which are given in the figures) are practically the same. The shown spectra verify the broad and continuous spectral nature of the MPC-31, which contrasts with the discrete spectrum of the PI-PWM control. In the latter case, some low-order harmonics exist in addition to the switching-frequency-related harmonics. They have been found to appear exactly at the frequencies of the rotor slot harmonics (which are rotor speed and stator fundamental frequency dependent [22]). On the other hand, these low-order harmonics are, in essence, absent for MPC-31, which means that the MPC-31 manages to suppress them. This proves that the FCS-MPC has a higher control bandwidth.

Fig. 13(c) shows the phase-a voltages of both control schemes for 30-Hz operation. The voltages are measured using a high-voltage differential probe and a 2.5-MHz oscilloscope (GW-Instek GDS-1062A). The corresponding FFT spectra (obtained using the MATLAB FFT) are shown in Fig. 13(d). Two very different voltage waveforms and spectra for the two control schemes stem from the distinctly different ways in which they control the VSI. For the MPC-31 case, there exist two dense regions of voltage harmonics around 1 and 5 kHz. This correlates well with the average switching frequency at this operating point, which is determined separately as 2.2 kHz. On the other hand, a typical PWM waveform results with PI-PWM control, and the spectrum contains the pronounced discrete harmonics in sidebands around the multiples of the switching frequency.

C. Transient Performance Comparison

Transient performance of the two control schemes in torque mode of operation is discussed. The total armature resistance of the dc generator is set to a high value, so that the load torque exerted on the induction motor is small. This gives a light-load operation (but with variable load torque) and thus faster speed transients. Current references for both schemes are set in the following manner: d-axis references (i^*_{sd} or i^*_{sd1}) are set to $\sqrt{2}$ A; q-axis current references (i^*_{sq} or i^*_{sq1}) are zero at time instant 0 s. Then, they are set to $2\sqrt{2}$ A, from 0.1

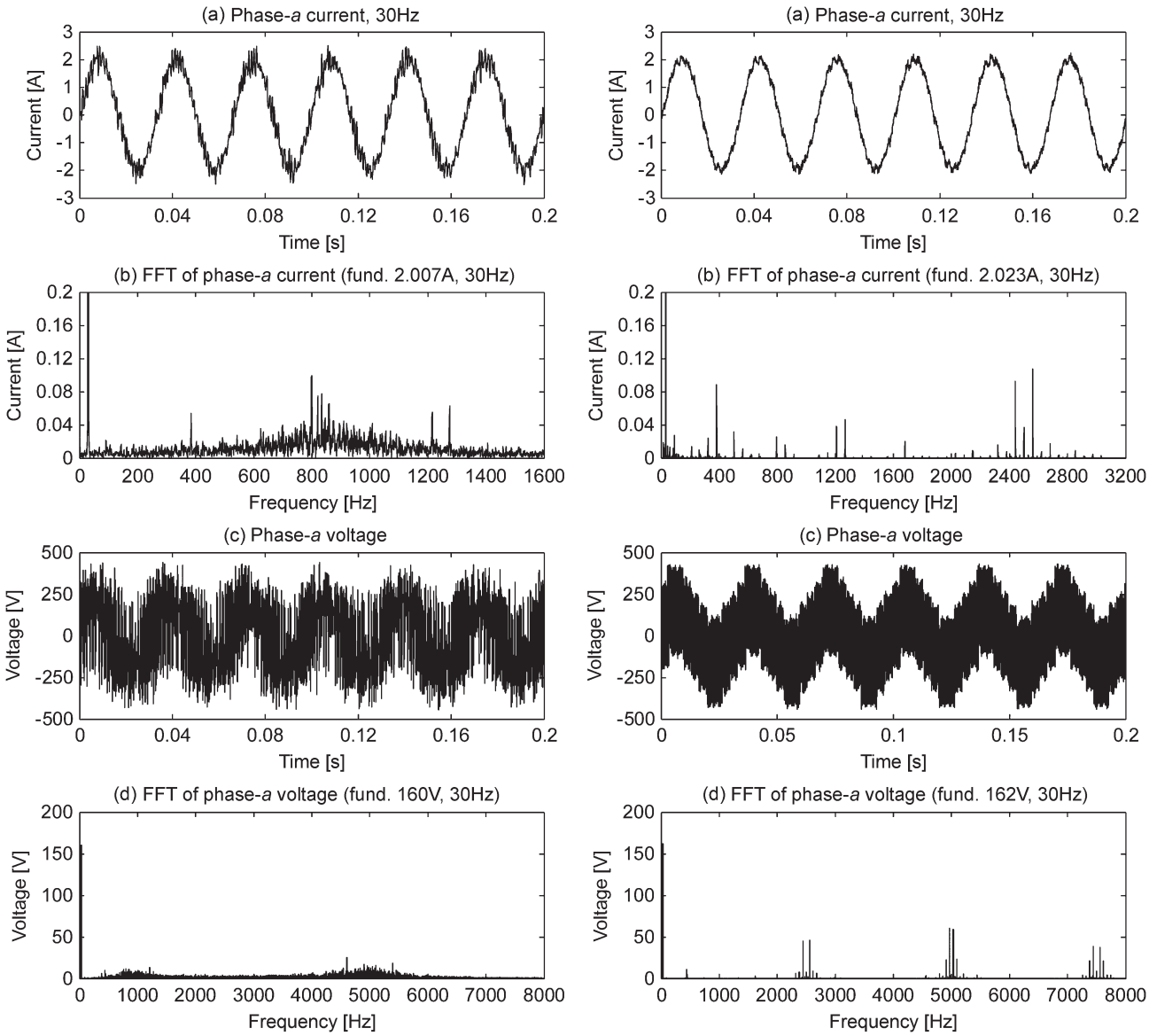

Fig. 13. (Experiment) Comparison of steady-state phase-a currents and voltages at 30-Hz operation. The machine is loaded with the same load torque as in Fig. 7. (a) Phase-a current waveform. (b) FFT of phase-a current. (c) Phase-a voltage waveform. (d) Corresponding FFT of the phase-a voltage. MPC-31 results are on the left, whereas PI-PWM results are on the right.

to 0.5 s, and are further stepped to $-2\sqrt{2}$ A to give a speed reversal. They remain constant from 0.5 to 1.1 s, and then, they are stepped back to $2\sqrt{2}$ A again. At 1.3 s, they are set to zero. It should be noted that the d-axis current is applied long before 0 s to establish the constant rotor flux before the torque command application. In addition, a higher magnitude of the q-axis current than the one used in previous study is used here, in order to give a faster speed transient. This is, however, followed by higher current ripples due to the increased rotor slot harmonics.

Fig. 14(a) shows the traces of the measured d- and q-axis currents during the experimental transient test for the MPC-31. The q-axis current exhibits a fast tracking response to the reference steps without any prolonged overshoot. In addition, the d-axis current is virtually undisturbed during the q-axis current transients. However, the ripple of the d-axis current is higher upon the injection of the q-axis current. This is caused by the existence of nonideal properties and the use of the single cost function governing all four current components. α-axis, x-axis, and phase-a currents are shown in Fig. 14(b) and (c). Similarly, the higher ripple of x-axis current is due to the previously mentioned reasons. The corresponding motor speed, as illustrated in Fig. 14(d), shows a near-linear speed response (the load torque is small, but is speed dependent).

The current and speed traces for the PI-PWM control are shown in Fig. 15. Fig. 15(a) reveals a very small interference between d- and q-axis currents during q-axis current steps, despite the inclusion of the dynamic decoupling terms. One may notice that the magnitude of the x-axis current becomes slightly larger during transients, e.g., around 0.5 s. This is explained by the smaller control bandwidth of PI controllers in regulating the disturbed secondary plane currents. Fig. 15(b) and (c) verify the presence of numerous nonideal properties, which have caused higher ripple in the x-axis and phase currents. Fig. 15(d) shows

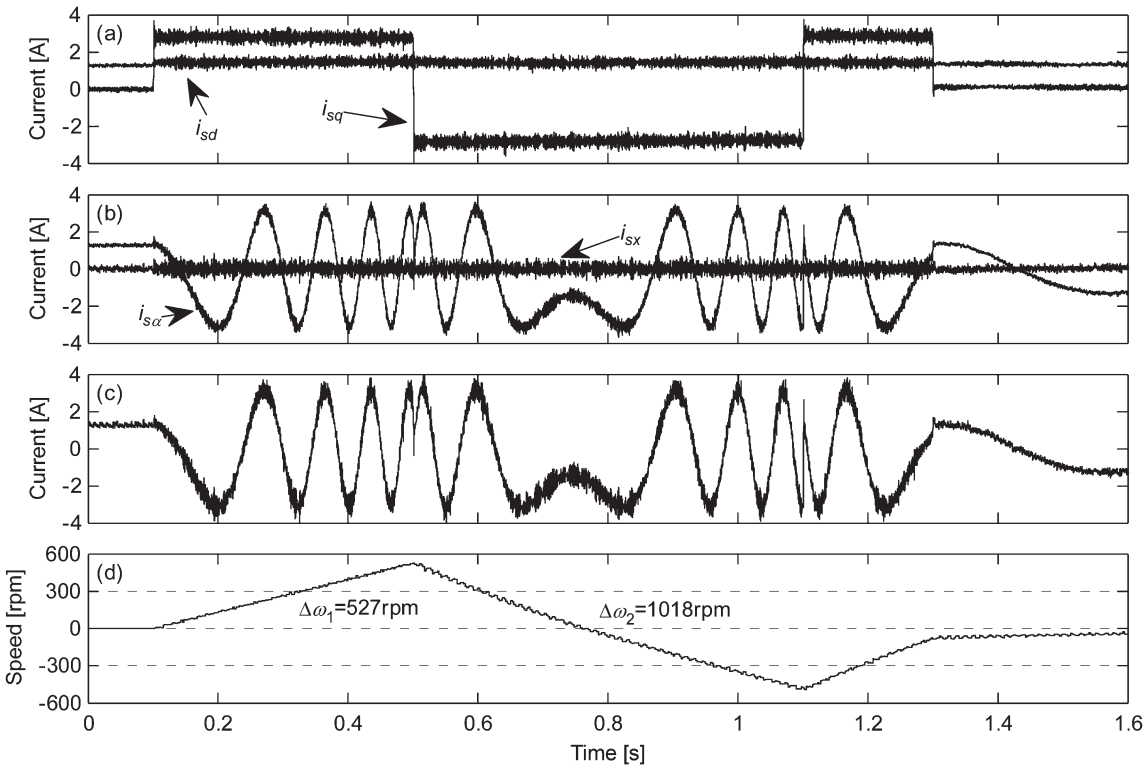

Fig. 14. (Experiment) Transient response of the MPC-31 for the current commands of $i^*_{sd} = \sqrt{2}$ A, $i^*_{sx} = i^*_{sy} = 0$ A, $i^*_{sq} = 0$ (0–0.1 s), $2\sqrt{2}$ A (0.1–0.5 s), $2\sqrt{2}$ A (0.5–1.1 s), $-2\sqrt{2}$ A (1.1–1.3 s), and finally 0 A (1.3–1.6 s). (a) i_{sd} and i_{sq}. (b) $i_{s\alpha}$ and i_{sx}. (c) Phase-a current. (d) Rotor speed.

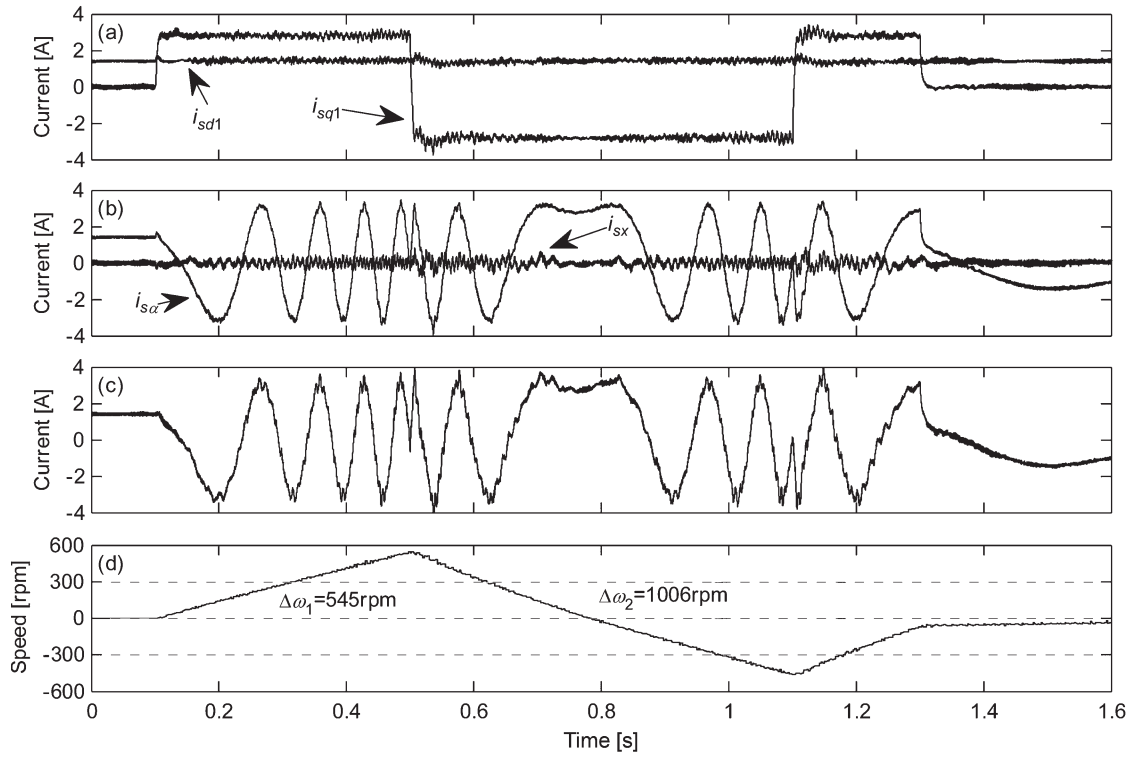

Fig. 15. (Experiment) Transient response of the PI-PWM control for the current commands of $i^*_{sd1} = \sqrt{2}$ A, $i^*_{sd2} = i^*_{sq2} = 0$ A, i^*_{sq1} is set in the same way as i^*_{sq} of the MPC-31 in Fig. 14. (a) i_{sd1} and i_{sq1}. (b) $i_{s\alpha}$ and i_{sx}. (c) Phase-a current. (d) Rotor speed.

a practically identical speed response as the one obtained for the MPC-31, although the PI-PWM control has slight overshoots and slower settling of the q-axis current.

Transient performance of the two schemes during q-axis current reversal (at $t = 0.5$ s) is illustrated further using zoomed extracts (see Fig. 16). The MPC-31 regulates the q-axis current

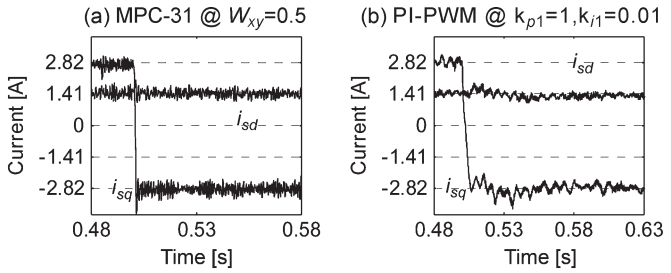

Fig. 16. Zoomed extracts around 0.5 s time instant for (a) MPC-31 and (b) PI-PWM control. A slower response and slight overshoot are seen in the synchronous $d-q$ currents of the PI-PWM control.

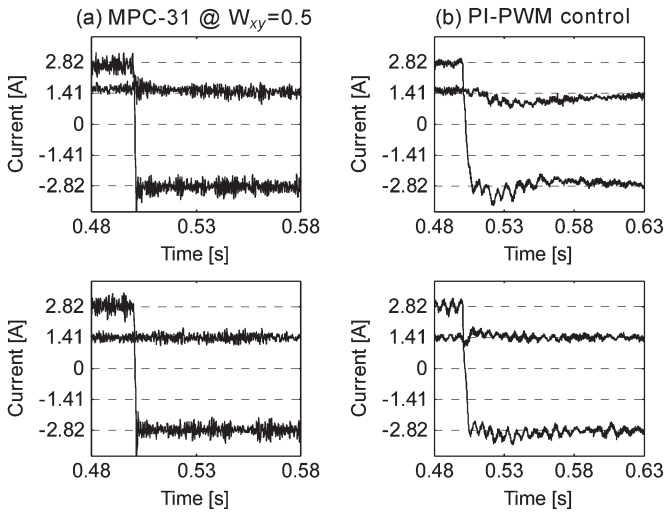

Fig. 17. (Experiment) Impact of incorrect rotor resistance setting on (a) MPC-31 and (b) PI-PWM control. Rotor resistance is set to 50% (upper graphs) and 150% (lower graphs) of the correct value. The same error was also introduced to the predictive model in MPC-31.

within 0.002 s, whereas the PI-PWM control needs about 0.05 s (accounting for the slow settling). It should be noted that this comparison has been made more reliable by tuning the PI controllers to give the best possible performance.

Since both control schemes rely on the slip speed estimation according to (5) for field orientation, the robustness of the control schemes against the slip speed estimation error is investigated next. The same transient test, as in Figs. 14 and 15, is repeated, this time, with the rotor resistance in (5) deliberately detuned by $\pm 50\%$ with respect to the correct value. The same rotor resistance detuning is also introduced in the predictive model of the MPC-31 scheme. Fig. 17 shows the experimental results. It appears in Fig. 17 that MPC-31's fast transient is hardly affected by the detuning. The same applies to PI-PWM control, except for the $+50\%$ value case, which results in slightly longer settling duration than when the value is correct (see Fig. 16). The problem with the results in Fig. 17 is that they show $d-q$ currents in the detuned reference frame, rather than in the true rotor-flux-oriented reference frame, and the two are not the same any more. Hence, to examine the behavior of the d- and q-axis in the true rotor-flux-oriented reference frame, results in Fig. 17 are complemented with the simulation results. Fig. 18 shows exactly the same traces for the same conditions as Fig. 17, but obtained by simulation. It is

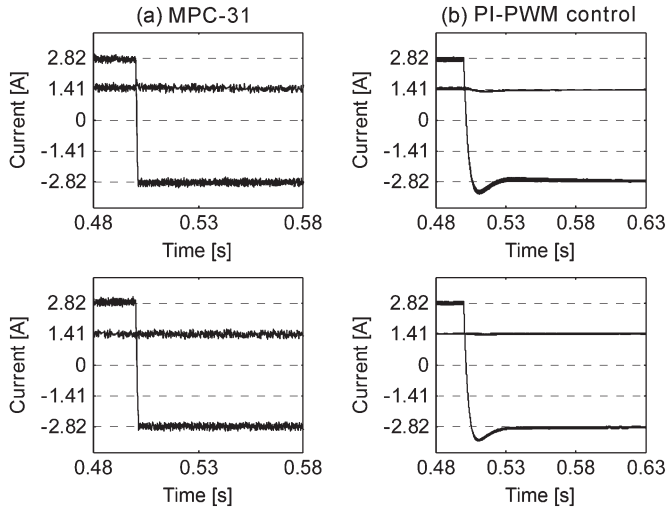

Fig. 18. (Simulation) Impact of incorrect rotor resistance setting on (a) MPC-31 and (b) PI-PWM control. Rotor resistance is set to 50% (upper graphs) and 150% (lower graphs) of the correct value. The same error was also introduced to the predictive model in MPC-31.

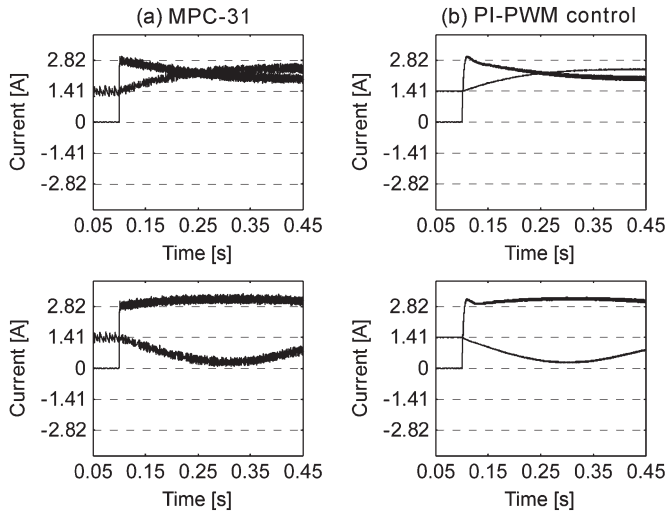

Fig. 19. (Simulation) Impact of incorrect rotor resistance setting on (a) MPC-31 and (b) PI-PWM control. Rotor resistance is set to 50% (upper graphs) and 150% (lower graphs) of the correct value. The same error was also introduced to the predictive model in MPC-31. True $d-q$ currents in the true rotor-flux-oriented reference frame are shown.

easy to ascertain that the agreement between Figs. 17 and 18 is rather good.

Hence, the simulation results of the true $d-q$ currents, shown in Fig. 19, can be regarded as representative of true currents in Fig. 17, for PI-PWM and MPC-31, and clearly show that the impact of the detuning is essentially the same in both control schemes, although, in the case of the MPC-31, detuning is additionally present in the predictive model as well. Such a behavior also fully validates the induction machine model used as the basis for the MPC, which is formulated in the rotor-flux-oriented reference frame without the q-axis rotor flux component.

Finally, a summary of the comparison of current control based on PI-PWM and FCS-MPC, together with some other relevant aspects, is given in Table V.

TABLE V
EXPERIMENTAL COMPARISON OF CURRENT CONTROL TECHNIQUES

Feature	PI-PWM control	MPC-31
Sampling freq.	2.5 kHz	10 kHz
Switching freq. (exp.)	2500 Hz	1950-3700 Hz
Dynamic decoupling	External	Internal
Machine parameter requirements	All except stator resistances	All
Control of the secondary plane currents	Additional pair of PI controllers	Current error in the single cost function
Computational cost	Low, 27μs	High, 82μs
Tuning	Difficult, retuning is required for different operating points	Easy, retuning is not required
Phase voltage/current spectra and THD	Modulation type, low THD (6.4% - 6.9%)	Broad and continuous, high THD (10.8% - 12.6%)
Transient, 90% rise time (in Fig. 16)	Slower, 4.5ms	Consistently faster, 0.7ms
Current control bandwidth	Smaller	Larger

V. CONCLUSION

The impact of using subsets of the complete inverter switching state set as the control input of FCS-MPC is studied first. The three considered sets are MPC-31, MPC-21, and MPC-11. In spite of numerous nonideal properties in the experiment, both simulation and experimental studies agree with each other very well, with regard to trends exhibited by the various current ripples in all three schemes.

All the schemes have similar ranges of average switching frequencies in the simulations, as well as in the experiments, with the experimental values being significantly higher.

It is shown that the MPC-31 and MPC-21 give practically the same current ripple performance, which is better than with the MPC-11. However, in order to reduce the computational time, one does not need to consider all the states as in MPC-31, since the reduced set of MPC-21 suffices. As the phase number increases, the number of states that have to be included in the MPC will increase, but there will never be a need to use all the states. For example, in a seven-phase system, there are 128 states, but FCS-MPC will give the same ripple characteristics regardless of whether all 128 states are used or a reduced set of 43 states is considered.

Next, there is flexibility in selecting the secondary plane current ripple weighting factor W_{xy} for MPC-21 and MPC-31, whereas MPC-11 can be used for the sake of minimum implementation cost under the equal weighting condition, i.e., with $W_{xy} = 1$ (but with consistently higher current ripple than MPC-21 and MPC-31, despite applying only small-magnitude $x-y$ voltage vectors).

A comparison of the FCS-MPC and the standard PI-PWM current control performance is presented next. On average, the MPC-31 gives 80% higher average phase current ripple than the PI-PWM control in the experiments. This value is higher than the one given by the flux/torque control using FCS-MPC in a three-phase induction motor drive, i.e., about 20% [23]. This is so, since PI-PWM in multiphase drives can easily achieve practically zero average voltage values in all planes other than the first, whereas FCS-MPC always applies a single switching state, thus inevitably causing excitation of the secondary plane(s). The current ripple of FCS-MPC can be improved by using a higher sampling frequency. This would, however, lead to a higher switching stress and would also be difficult to achieve with higher phase numbers, due to the increase in the number of switching states and hence computational burden on the DSP.

The MPC-31 shows a consistently faster current tracking than the PI-PWM control. Tuning of the controller is significantly easier than that of PI controllers. Additionally, the MPC-31 has a much wider current control bandwidth compared with the PI controllers, as shown by the ability to mitigate the low-order rotor-slot-induced current harmonics (below about 200 Hz). The rotor resistance detuning study has shown that the behavior of both current control schemes is dominated by the detuning in the rotor angular speed calculations and is therefore very much the same.

REFERENCES

[1] E. Levi, R. Bojoi, F. Profumo, H. A. Toliyat, and S. Williamson, "Multiphase induction motor drives—A technology status review," *IET Electric Power Appl.*, vol. 1, no. 4, pp. 489–516, Jul. 2007.

[2] E. Levi, "Multiphase electric machines for variable-speed applications," *IEEE Trans. Ind. Electron.*, vol. 55, no. 5, pp. 1893–1909, May 2008.

[3] J. Rodriguez and P. Cortes, *Predictive Control of Power Converters and Electrical Drives*. Hoboken, NJ, USA: Wiley, 2012.

[4] M. R. Arahal, F. Barrero, S. Toral, M. Duran, and R. Gregor, "Multi-phase current control using finite-state model-predictive control," *Control Eng. Pract.*, vol. 17, no. 5, pp. 579–587, May 2009.

[5] F. Barrero, M. R. Arahal, R. Gregor, S. Toral, and M. J. Duran, "A proof of concept study of predictive current control for VSI-driven asymmetrical dual three-phase AC machines," *IEEE Trans. Ind. Electron.*, vol. 56, no. 6, pp. 1937–1954, Jun. 2009.

[6] F. Barrero, M. R. Arahal, R. Gregor, S. Toral, and M. J. Duran, "One-step modulation predictive current control method for the asymmetrical dual three-phase induction machine," *IEEE Trans. Ind. Electron.*, vol. 56, no. 6, pp. 1974–1983, Jun. 2009.

[7] R. Gregor, F. Barrero, S. L. Toral, M. J. Duran, M. R. Arahal, J. Prieto, and J. L. Mora, "Predictive-space vector PWM current control method for asymmetrical dual three-phase induction motor drives," *IET Electric Power Appl.*, vol. 4, no. 1, pp. 26–34, Jan. 2010.

[8] F. Barrero, J. Prieto, E. Levi, R. Gregor, S. Toral, M. Duran, and M. Jones, "An enhanced predictive current control method for asymmetrical six-phase motor drives," *IEEE Trans. Ind. Electron.*, vol. 58, no. 8, pp. 3242–3252, Aug. 2011.

[9] M. J. Duran, J. Prieto, F. Barrero, and S. Toral, "Predictive current control of dual three-phase drives using restrained search techniques," *IEEE Trans. Ind. Electron.*, vol. 58, no. 8, pp. 3253–3263, Aug. 2011.

[10] J. A. Riveros, F. Barrero, E. Levi, M. Duran, S. Toral, and M. Jones, "Variable-speed five-phase induction motor drive based on predictive torque control," *IEEE Trans. Ind. Electron.*, vol. 60, no. 8, pp. 2957–2968, Aug. 2013.

[11] C. S. Lim, N. A. Rahim, W. P. Hew, M. Jones, and E. Levi, "Model predictive current control of a five-phase induction motor," in *Proc. IEEE IECON*, Melbourne, Vic, Australia, 2011, pp. 1934–1940.

[12] C. S. Lim, N. A. Rahim, W. P. Hew, M. Jones, and E. Levi, "Experimental evaluation of model predictive current control of a five-phase induction motor using all switching states," in *Proc. Int. Conf. EPE-PEMC*, Novi Sad, Serbia, 2012, pp. LS1c.4-1–LS1c.4-7, [CD-ROM].

[13] A. Iqbal, H. Abu-Rub, P. Cortés, and J. Rodriguez, "Finite control set model predictive current control of a five-phase voltage source inverter," in *Proc. IEEE ICIT*, Viña del Mar, Chile, 2010, pp. 1787–1792.

[14] P. Cortés, L. Vattuone, J. Rodriguez, and M. Duran, "A method of predictive current control with reduced number of calculations for five-phase voltage source inverters," in *Proc. IEEE IECON*, Porto, Portugal, 2009, pp. 53–58.

[15] C. S. Lim, N. A. Rahim, W. P. Hew, and E. Levi, "Model predictive control of a two-motor drive with five-leg inverter supply," *IEEE Trans. Ind. Electron.*, vol. 60, no. 1, pp. 54–65, Jan. 2013.

[16] A. Iqbal and E. Levi, "Space vector PWM techniques for sinusoidal output voltage generation with a five-phase voltage source inverter," *Elect. Power Compon. Syst.*, vol. 34, no. 2, pp. 119–140, Feb. 2006.
[17] E. S. de Santana, E. Bim, and W. C. do Amaral, "A predictive algorithm for controlling speed and rotor flux of induction motor," *IEEE Trans. Ind. Electron.*, vol. 55, no. 12, pp. 4398–4407, Dec. 2008.
[18] M. Jones, S. N. Vukosavic, D. Dujic, and E. Levi, "A synchronous current control scheme for multiphase induction motor drives," *IEEE Trans. Energy Convers.*, vol. 24, no. 4, pp. 860–868, Dec. 2009.
[19] S. Kouro, P. Cortés, R. Vargas, U. Ammann, and J. Rodriguez, "Model predictive control—A simple and powerful method to control power converters," *IEEE Trans. Ind. Electron.*, vol. 56, no. 6, pp. 1826–1838, Jun. 2009.
[20] P. Cortés, A. Wilson, J. Rodriguez, S. Kouro, and H. Abu-Rub, "Model predictive control of multilevel cascaded H-bridge inverters," *IEEE Trans. Ind. Electron.*, vol. 57, no. 8, pp. 2691–2699, Aug. 2010.
[21] M. Jones, D. Dujic, E. Levi, J. Prieto, and F. Barrero, "Switching ripple characteristics of space vector PWM schemes for five-phase two-level voltage source inverters—Part 2: Current ripple," *IEEE Trans. Ind. Electron.*, vol. 58, no. 7, pp. 2799–2808, Jul. 2011.
[22] P. Vas, *Parameter Estimation, Condition Monitoring, and Diagnosis of Electrical Machines*. New York, NY, USA: Oxford Univ. Press, 1993.
[23] J. Rodriguez, R. M. Kennel, J. R. Espinoza, M. Trincado, C. A. Silva, and C. A. Rojas, "High-performance control strategies for electrical drives: An experimental assessment," *IEEE Trans. Ind. Electron.*, vol. 59, no. 2, pp. 812–820, Feb. 2012.

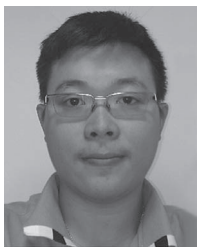

Chee Shen Lim (S'10) received the B.Eng. degree (Hons.) in electrical engineering from the University of Malaya, Kuala Lumpur, Malaysia, in 2009. He is currently working toward the joint-university Ph.D. degree at the University of Malaya and Liverpool John Moores University, Liverpool, U.K.

Since 2009, he has been a Research Assistant with the Power Energy Dedicated Advanced Center (UMPEDAC), University of Malaya. His research interests include high-performance drives and embedded real-time control.

Emil Levi (S'89–M'92–SM'99–F'09) received the M.Sc. and Ph.D. degrees from the University of Belgrade, Belgrade, Serbia, in 1986 and 1990, respectively.

From 1982 to 1992, he was with the Department of Electrical Engineering, University of Novi Sad, Novi Sad, Serbia. In May 1992, he joined Liverpool John Moores University, Liverpool, U.K., where he has been a Professor in electric machines and drives, since September 2000.

Dr. Levi serves as Coeditor-in-Chief of the IEEE TRANSACTIONS ON INDUSTRIAL ELECTRONICS, as an Editor of the IEEE TRANSACTIONS ON ENERGY CONVERSION, and as Editor-in-Chief of IET *Electric Power Applications*. He was the recipient of the Cyril Veinott Award of the IEEE Power and Energy Society in 2009.

Martin Jones received the B.Eng. degree (First Class Honors) in electrical engineering and the Ph.D. degree from Liverpool John Moores University, Liverpool, U.K., in 2001 and 2005, respectively.

From September 2001 to Spring of 2005, he was a Research Student with Liverpool John Moores University, where he currently serves as a Reader. His research is in the area of high-performance ac drives.

Dr. Jones was a recipient of the IEE Robinson Research Scholarship for his Ph.D. studies.

Nasrudin Abd. Rahim (M'89–SM'08) received the B.Sc. (Hons.) and M.Sc. degrees from the University of Strathclyde, Glasgow, U.K. He received the Ph.D. degree from Heriot–Watt University, Edinburgh, U.K., in 1995.

He is currently a Professor with the Faculty of Engineering, University of Malaya, Kuala Lumpur, Malaysia, where he is also the Director of the Power Energy Dedicated Advanced Center (UMPEDAC).

Prof. Rahim is a Fellow of The Institution of Engineering and Technology, U.K., and the Academy of Sciences Malaysia.

Wooi Ping Hew (M'06) received the B.Eng. and Masters' (Electrical) degrees from the Universiti Tekonologi Malaysia, Johor Bahru, Malaysia. He received the Ph.D. degree from the University of Malaya, Kuala Lumpur, Malaysia, in 2000.

He is currently a Professor with the Faculty of Engineering, University of Malaya. His research interests include electrical drives and electrical machine design.

Dr. Hew is a member of The Institution of Engineering and Technology, U.K., and a Chartered Engineer in the U.K.